ADVANCED MATERIALS
www.advmat.de

High-Stroke, High-Output-Force, Fabric-Lattice Artificial Muscles for Soft Robots

*Dezhi Yang, Miao Feng, and Guoying Gu**

Artificial muscles, providing safe and close interaction between humans and machines, are essential in soft robotics. However, their insufficient deformation, output force, or configurability usually limits their applications. Herein, this work presents a class of lightweight fabric-lattice artificial muscles (FAMs) that are pneumatically actuated with large contraction ratios (up to 87.5%) and considerable output forces (up to a load of 20 kg, force-to-weight ratio of over 250). The developed FAMs consist of a group of active air chambers that are zigzag connected into a lattice through passive connecting layers. The geometry of these fabric components is programmable to convert the in-plane lattice of FAMs into out-of-plane configurations (e.g., arched and cylindrical) capable of linear/radial contraction. This work further demonstrates that FAMs can be configured for various soft robotic applications, including the powerful robotic elbow with large motion range and high load capability, the well-fitting assistive shoulder exosuit that can reduce muscle activity during abduction, and the adaptive soft gripper that can grasp irregular objects. These results show the unique features and broad potential of FAMs for high-performance soft robots.

1. Introduction

Artificial muscles, made from flexible materials and structures, are well suited to perform compliant actuation due to their ability to conform to surroundings and are promising in human-friendly soft robotics,[1] including biomimetic robots,[2–4] wearable devices,[5,6] and operation machines.[7,8] During the past decade, numerous artificial muscles have been developed based on 1) new materials, such as hydrogel actuators,[9,10] dielectric/liquid crystal elastomer actuators,[11–15] shape memory alloys/polymers,[16,17] and piezoelectric actuators,[18,19] and 2) novel structures, such as twisted string actuators,[20,21] hydraulically amplified self-healing electrostatic actuators,[22,23] and pneumatic/hydraulic artificial muscles.[24–27] Although these artificial muscles show particular merits in some aspects, their practical applications are generally limited by insufficient deformation, output force, or configurability.

Among existing artificial muscles, pneumatic artificial muscles (PAMs) are the most prevailing, owing to their safety, simplicity, low cost, and ease of implementation. The well-known McKibben PAMs, invented in the 1950s, can achieve muscle-like linear contraction with blocking forces of hundreds of Newtons.[28,29] Nevertheless, they suffer from a limited contraction ratio of less than 36%. To improve the contraction performance, a range of McKibben variants are proposed, including the pleated pneumatic artificial muscles,[30,31] origami actuators,[32] chain-link actuators,[33] flat inflatable artificial muscles,[34] and these paired and gusseted pouch motors.[35,36] These PAMs can achieve a maximum contraction ratio of up to 65%;[37,38] however, their configuration and actuation (i.e., contraction) are monotonous, limiting their applications in complex architectures and motions.

In tackling these challenges, many efforts have also been dedicated to enriching the configurations and actuation modes of PAMs, such as contraction, extension, bending, twisting, and their hybrid. Typical methods include 1) varying the arrangements of strain-limiting components (e.g., fibers),[39–42] 2) tuning the geometry of air chambers,[43,44] 3) introducing air chamber arrays.[45,46] However, their output force and contraction ratio are usually limited. Some recently reported methods for configuration advantages[47,48] can concurrently improve the maximum contraction ratio to 71%[48] by integrating the rigid path shells, which, however, increase the complexity and reduce the compliance. Notably, vacuum-based artificial muscles can achieve a state-of-the-art contraction ratio of over 90%[49,50] and programmable motions by shaping the embedded compressible skeletons.[49] However, vacuum actuation is usually inefficient and has limited actuation pressure of less than one atmosphere. Therefore, it remains an open challenge to design PAMs with

D. Yang, M. Feng, G. Gu
Robotics Institute
School of Mechanical Engineering
Shanghai Jiao Tong University
Shanghai 200240, China
E-mail: guguoying@sjtu.edu.cn
D. Yang, M. Feng, G. Gu
State Key Laboratory of Mechanical System and Vibration
Shanghai Jiao Tong University
Shanghai 200240, China
G. Gu
Meta Robotics Institute
Shanghai Jiao Tong University
Shanghai 200240, China

The ORCID identification number(s) for the author(s) of this article can be found under https://doi.org/10.1002/adma.202306928

DOI: 10.1002/adma.202306928

large deformation, high output forces, and diverse configurations and motions.

Here, we introduce a class of lightweight fabric-lattice artificial muscles (FAMs) by zigzag connecting a group of active fabric air chambers and passive fabric connecting layers into a lattice. The loose lattice structures and the flexible fabric materials together endow the FAMs with excellent structural stretchability and abundant design extendibility. The force–contraction relations of FAMs can be tuned by adjusting the actuation unit parameters based on our simplified model, which can achieve a large contraction ratio of 87.5% and a high force-to-weight ratio of over 250 (capable of lifting a load of 20 kg). By programming the geometry of the air chamber and connecting layer, the in-plane lattice of FAMs can be further morphed into desired out-of-plane configurations, such as arched and cylindrical, to perform linear or radial contraction. These unique features enable FAMs to show excellent potential in high-performance soft robots, such as an antagonistic robotic elbow with large motion range (260°) and high load capability (>1 kg), a well-fitting assistive shoulder exosuit that can reduce the muscle activity (34.4% for the medial deltoid) during abduction, and an adaptive soft gripper that can grasp irregular objects by self-adapting to their surfaces.

2. Results

2.1. Design and Working Principle of FAMs

Figure 1a–c illustrates the structures and working principles of FAMs, which have a shape of a hollow rhombic lattice and perform muscle-like contraction under increasing actuation pressure. Here, one FAM consists of multiple cascaded row arrays (Figure 1a), and each row array is composed of an active air chamber and a passive connecting layer (Figure 1b). The air chamber and connecting layer are both made from lightweight heat-sealable fabrics (Note S1 and Figure S1, Supporting Information) and then connected in a mirror zigzag pattern at specified locations through heat-pressing (Note S2, Figures S2 and S3, and Movie S1, Supporting Information). In a row array, the basic rhombic actuation unit locates between each two adjacent heat-pressing areas (Figure 1c).

When depressurized, the actuation unit exhibits large stretchability due to the flexibility of the fabrics. Thus, the actuation unit can be stretched vertically with a small preload, creating a slender rhombus shape. When pressurized, the air chamber rapidly expands, stiffens, and straightens, producing torque at the crease. As a result, the actuation unit elongates horizontally and contracts vertically, evolving into a flat rhombus shape. Specifically, the vertical length of the actuation unit gradually decreases from $2l$ to a theoretical minimum value of $\frac{2w}{\pi}$, where l is the side length of the actuation unit and w is the width of the air chamber. Regarding $2l$ as the original length, the maximum contraction ratio $\epsilon_{\max}$ can be obtained as

$$\epsilon_{\max} = 1 - \frac{w}{\pi l} \tag{1}$$

which ranges from 0% to 100% in theory since the geometric parameters w and l are independent.

It is worth noting that these actuation units in the same row array share one long air chamber (Figure 1b), which will introduce additional creases between each two actuation units to enhance the output force. In this work, an FAM typically consists of five row arrays, and each row array has three actuation units. Figure 1d shows that the normal prototype of FAM (w = 33 mm, l = 35 mm, 56.2 g, chamber volume = 404.3 cm^3) can reach a contraction of 65.0% with a load of 2 kg under 200 kPa. Through tuning the geometric parameters, FAMs can also achieve a high-contraction-ratio prototype (w = 23 mm, l = 80 mm, 36.4 g, chamber volume = 164.8 cm^3) with a contraction ratio of 87.5% (Figure 1e and Movie S2, Supporting Information) and a high-output-force prototype (w = 53 mm, l = 35 mm, 80.0 g, chamber volume = 1116.2 cm^3) capable of lifting a load of 20 kg (250 times its weight, corresponding to a high energy density of 286 J kg^{-1}) under 200 kPa (Figure 1f and Movie S2, Supporting Information).

2.2. Performance Characterization of FAMs

To investigate the influence of the geometric parameters (i.e., the w and l) on the performance, we design, fabricate, and characterize nine types of FAMs with varying dimensions (**Figure 2**a and Figure S4, Supporting Information). The w and l of these FAMs are 23, 28, 33 mm and 25, 30, 35 mm respectively (the normal prototype belongs to type IX) (Table S1, Supporting Information). The expanded chamber volumes of these FAMs are between 89.4 and 404.3 cm^3 (Note S3, Supporting Information), and they all have a natural length of approximately 40 mm.

We first characterize the resistance force when stretching these FAMs to the prescribed original length ($10l$ for the FAMs, consistent with $2l$ for the actuation unit) by passive tensile tests (Note S4 and Figure S5, Supporting Information) and note the resistance force at the prescribed original length as the preload. The results show that the resistance force keeps a low level before approaching the prescribed original length, where it increases sharply due to the transition from structural deformation to material deformation (Figure 2b). Moreover, the preload is between 10 and 20 N and slightly increases with w and l (Table S1, Supporting Information).

We then measure the force–contraction relations of these nine types of FAMs from 0 to 150 kPa (Note S5 and Figure S6, Supporting Information), which agree well with the predictions of our simplified model in most cases (Figure 2c, Note S6, and Figures S7 and S8, Supporting Information). Experimental results show that the output forces of the FAMs 1) are almost proportional to the actuation pressure, 2) generally decrease with contraction, 3) typically decrease slowly in the middle stage of contraction, and 4) mostly maintain a considerable value at a large contraction ratio (>45%). This unique trend of force–contraction relation may be due to the increase in bending stiffness of the air chamber during contraction alleviating the decrease of output force.

We further extract the maximum contraction ratio and the prescribed average stress (to compare the output force fairly) for each type of FAM from the force–contraction relations under 150 kPa (see Note S7, Supporting Information). On the one hand, the maximum contraction ratio distributes between 30% and 80% and decreases linearly with $\frac{w}{l}$, which is consistent with Equation (1) (Figure 2d). On the other hand, the prescribed average stress increases with $\frac{w}{l}$ on the whole, which can be well predicted by our model when $\frac{w}{l}$ is less than 1.53 (Figure 2e). The errors

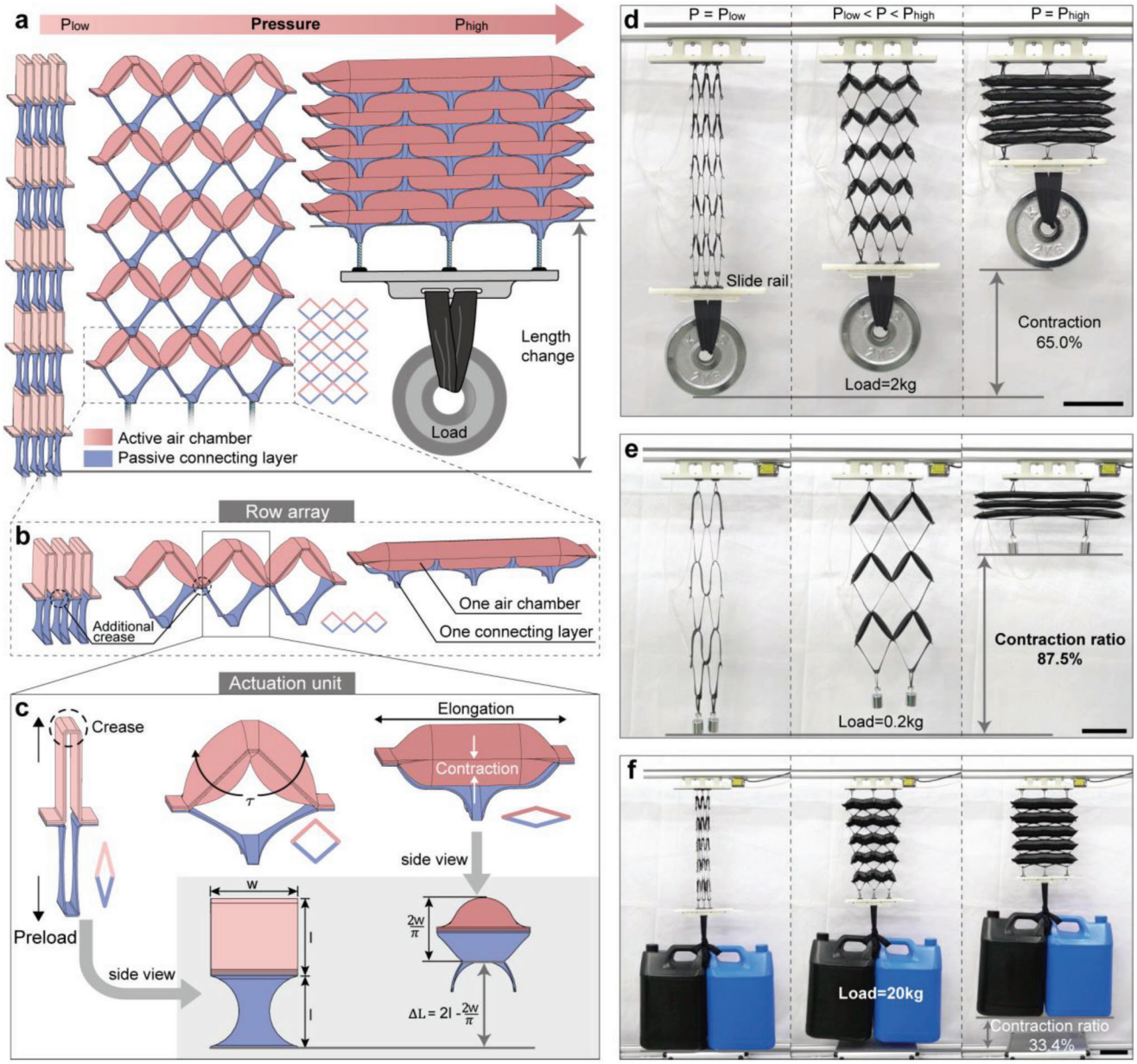

Figure 1. Design and working principle of fabric-lattice artificial muscles (FAMs). a) Schematic diagram of a five-row-array FAM with muscle-like contraction behaviors under increasing actuation pressure. b) Each row array consists of an active air chamber and a passive connecting layer; basic rhombic actuation units locate between each two adjacent heat-pressing areas. c) The working principle of the rhombic actuation unit. d) A normal prototype ($w = 33$ mm, $l = 35$ mm, 56.2 g, chamber volume = 404.3 cm^3) reaches a contraction ratio of 65% with a load of 2 kg. e) A large-contraction-ratio prototype ($w = 23$ mm, $l = 80$ mm, 36.4 g, chamber volume = 164.8 cm^3) reaches a contraction ratio of 87.5% with a load of 0.2 kg. f) A high-output-force prototype ($w = 53$ mm, $l = 35$ mm, 80.0 g, chamber volume = 1116.2 cm^3) lifts a load of 20 kg with a contraction ratio of 33.4%. The actuation pressure is all 200 kPa. Scale bars, 10 cm.

between the experiment and our model may be attributed to the deformation impediment of the connecting layer when $\frac{w}{l}$ is too large. Accordingly, the performance of FAMs (i.e., the maximum contraction ratio and the prescribed average stress) can be governed by the ratio $\frac{w}{l}$ and there is a trade-off between them.

We also conduct the load lifting and cyclic tests on the FAMs (Note S8, Figure S9, and Movie S2, Supporting Information). Experimental results show that the FAM (type IX) can lift a load of 5, 7.5, and 10 kg with a contraction ratio of 61.4%, 55.6%, and 45.4% under 200 kPa, corresponding to the energy density of 187, 255, and 277 J kg^{-1}, demonstrating its capability to lift heavy load with large contraction ratios. For the cyclic test, we apply a sinusoidal pressure (0–80 kPa, 0.2 Hz) to actuate an FAM (type IX) with a load of 3.5 kg. The stroke decreases from 129 mm (36.9%) to 114 mm (32.6%) due to fatigue after 5000 cycles (Figure 2f), but no air leakage or permanent damage is observed during the test, including the connections between the air chambers and connecting layers, which indicate that our FAMs possess robust

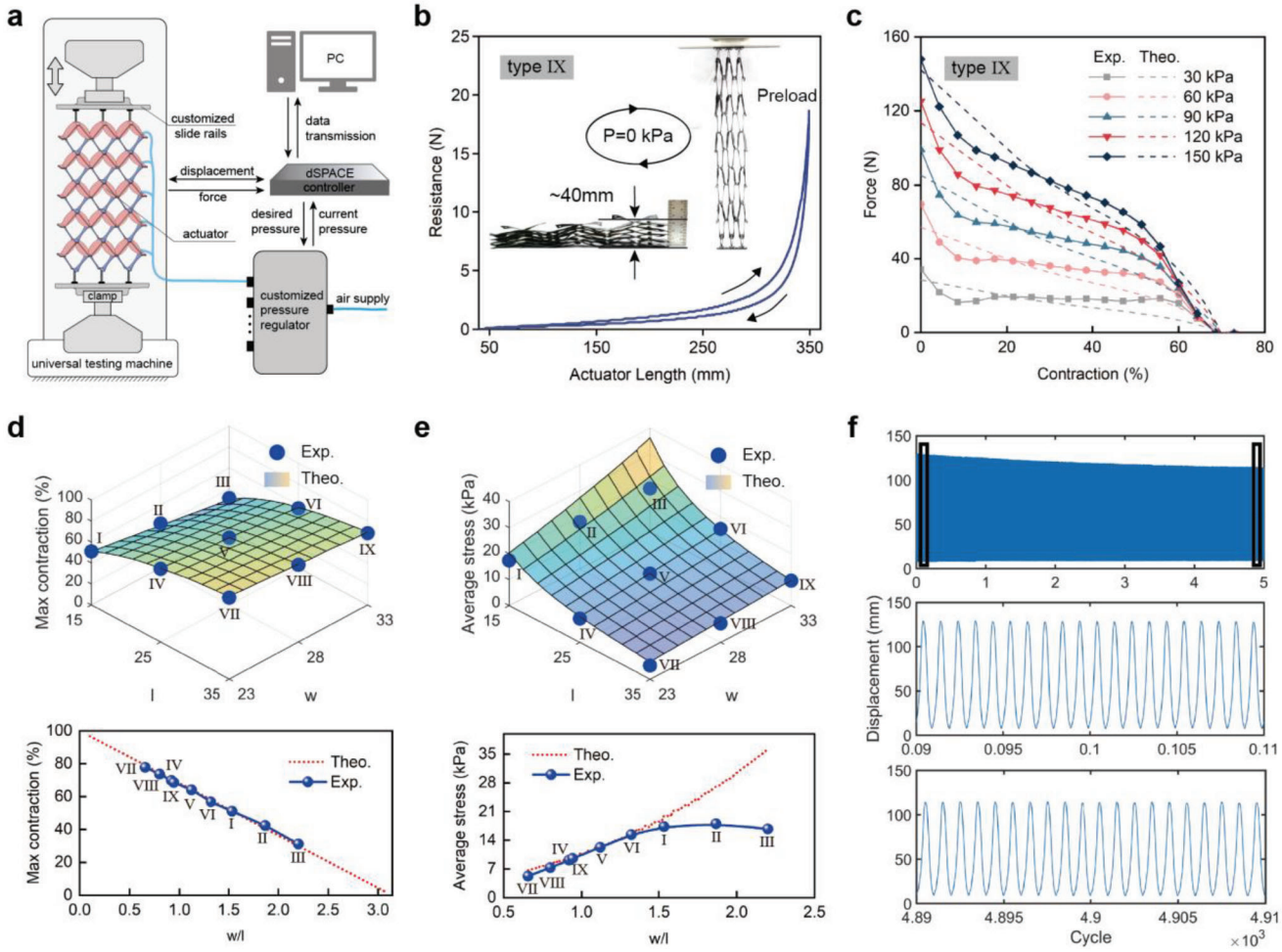

Figure 2. Performance characterization of fabric-lattice artificial muscles (FAMs). a) Experiment setup for the passive tensile test and force–contraction relation characterization. b) Passive tensile test result of the FAM (type IX). c) Force-contraction relations of the FAM (type IX), comparing with theoretical calculation results. d) The maximum contraction ratio of the nine types of FAMs. e) The prescribed average stress of the nine types of FAMs. f) Cyclic test results of the FAM (type IX) with a load of 3.5 kg under a sinusoidal pressure (0–80 kPa, 0.2 Hz).

longevity for practical applications with large stroke and heavy load.

2.3. Application I: A Biomimetic Robotic Elbow Based on FAMs

The exceptional contraction ratio and output force of FAMs make them ideal for use in biomimetic robots. By mimicking the movements of the human biceps and triceps brachialis (**Figure 3**a), we design a robotic elbow (838.9 g) in human elbow size by antagonistically arranging a pair of FAMs (type V) across a hinge (Figure 3b, Note S9, Figure S10a, Movie S3, Supporting Information). The robotic elbow can flex in both directions, covering a wide motion range spanning from −128° to 132° (Figure 3c). Holding a load of 1 kg in "hand," it can still move between −105° and 105° (actuation pressure = 0–200 kPa) (Figure 3d). Based on the simple PI controller and feedforward controller (Figure S10b, Supporting Information), we can control the flex angle of the robotic elbow and make it track desired angle signals, such as ramp and sinusoidal (Figure 3e,f). The tracking errors are 1.1°, 1.5°, and 3.1° (the average of absolute errors) for ramp angle signals with angular speeds of 1, 2, and 5 ° s^{-1}, and 22.8° phase lag for sinusoidal angle signals with an amplitude of 45° and a period of 20 s. Under an approximate step stimulus of pressure (100 kPa), the robotic elbow can throw out a ping-pong ball (2.7 g) with an initial velocity of 2.86 m s^{-1} (Figure 3g and Figure S10c, Supporting Information). These results show that our robotic elbow performs well among existing related devices driven by soft actuators[21,23,35] and demonstrate the large contraction ratio, high output force, controllability, and rapid response of our FAMs.

2.4. Application II: An Assistive Shoulder Exosuit Based on Arched FAMs

Besides in-plane configuration, our FAMs can achieve desired out-of-plane configuration by tuning the geometry of air chambers and connecting layers. As shown in **Figure** 4a, the row array, consisting of the semicircle air chamber and semicircle

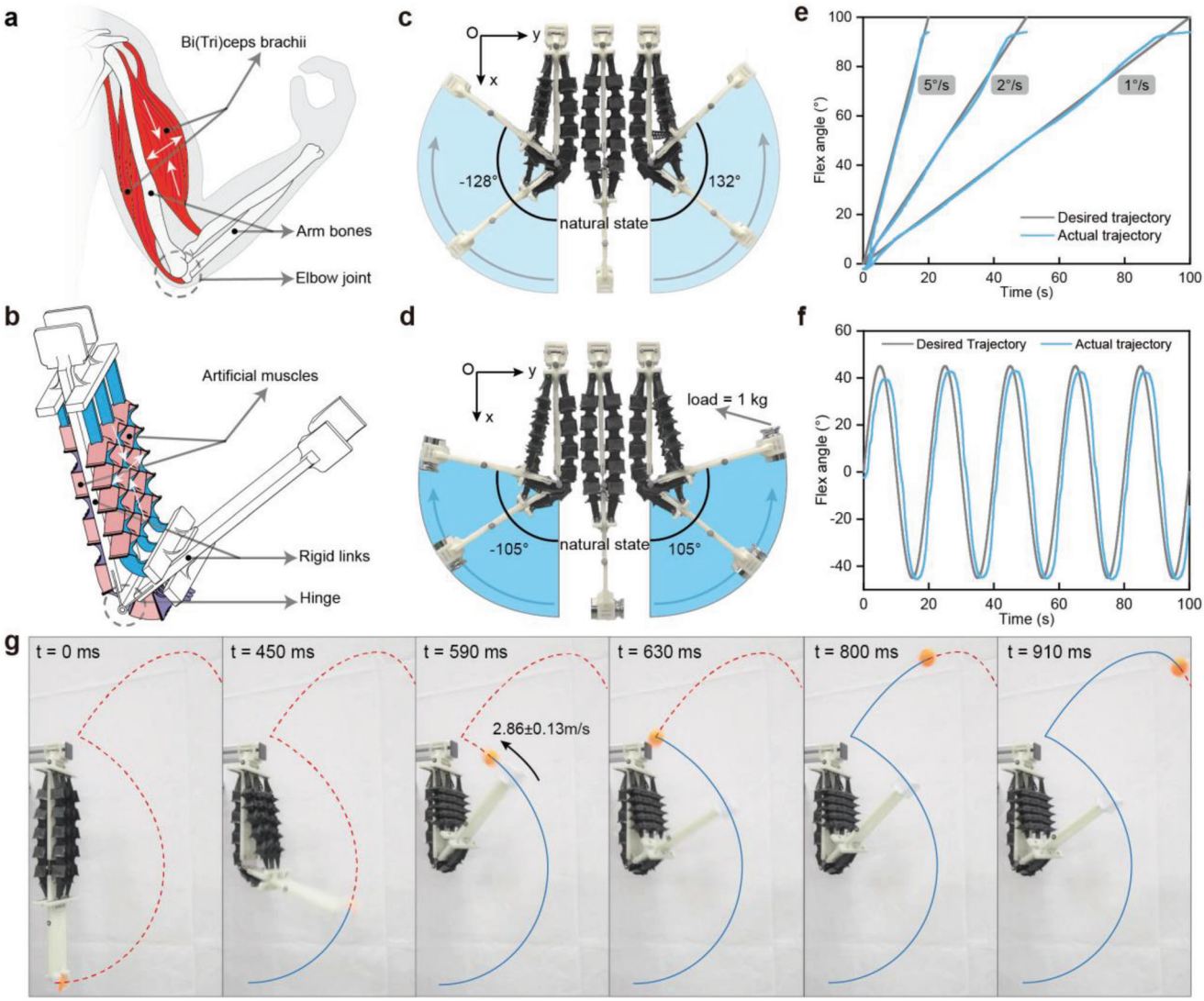

Figure 3. A biomimetic robotic elbow based on fabric-lattice artificial muscles (FAMs). a,b) Schematic diagram of the human elbow and the robotic elbow. c,d) Motion range of the robotic elbow without load and with a load of 1 kg (actuation pressure = 0–200 kPa). e,f) Performances of the robotic elbow when tracking ramp angle signals of various speeds and a sinusoidal angle signal with an amplitude of 45° and a period of 20 s. g) Under an approximate step pressure actuation (100 kPa), the FAM contracts fast enough to throw out a ping-pong ball (2.7 g) with an initial velocity of 2.86 ± 0.13 ms^{-1}.

connecting layer, can elongate along an arc and contract vertically when pressurized. The FAMs based on this row array can contract into an arched configuration with load-bearing capability (Figure S11a,b, Supporting Information), thus are termed arched FAMs (Movie S4, Supporting Information).

We then use the arched FAM (143.2 g, chamber volume = 1109.0 cm^3) to develop an assistive shoulder exosuit (412.3 g) (Figure 4b). To improve the stroke and output force, the arched FAM here includes 15 row arrays and each of them contains five actuation units. The semicircle air chambers are designed with an inner diameter of 110 mm, referencing the size of the human shoulder (Figure S3b, Supporting Information). Specifically, the arched FAM can be stretched to 530 mm with a preload of 13.8 N and contract to 269 mm when pressurized. To transmit the contraction force to the human arm, we attach the two ends of the arched FAM to the shoulder fabric base and the elbow fabric base (Figure S11c,d, Supporting Information) with fasteners. This design ensures that the shoulder exosuit is mechanically transparent when depressurized and fits snugly around the human shoulder when deforming.

The shoulder exosuit is first verified on a mannequin with a smooth spherical shoulder joint (Figure 4c, Note S10, and Movie S5, Supporting Information). When pressurized, the exosuit successively pulls the mannequin's arm up over the horizontal position, equivalent to applying torque larger than 4.5 N m at the shoulder joint. Experimental results show that the shoulder abduction angle (initial angle = 15.0°) is 105.0°, 91.9°, 60.1°, and 38.2° when the mannequin holds an additional load of 0, 0.5, 1, and 2 kg under 200 kPa (Figure 4d). A preliminary verification is then conducted on a healthy subject by comparing his muscle

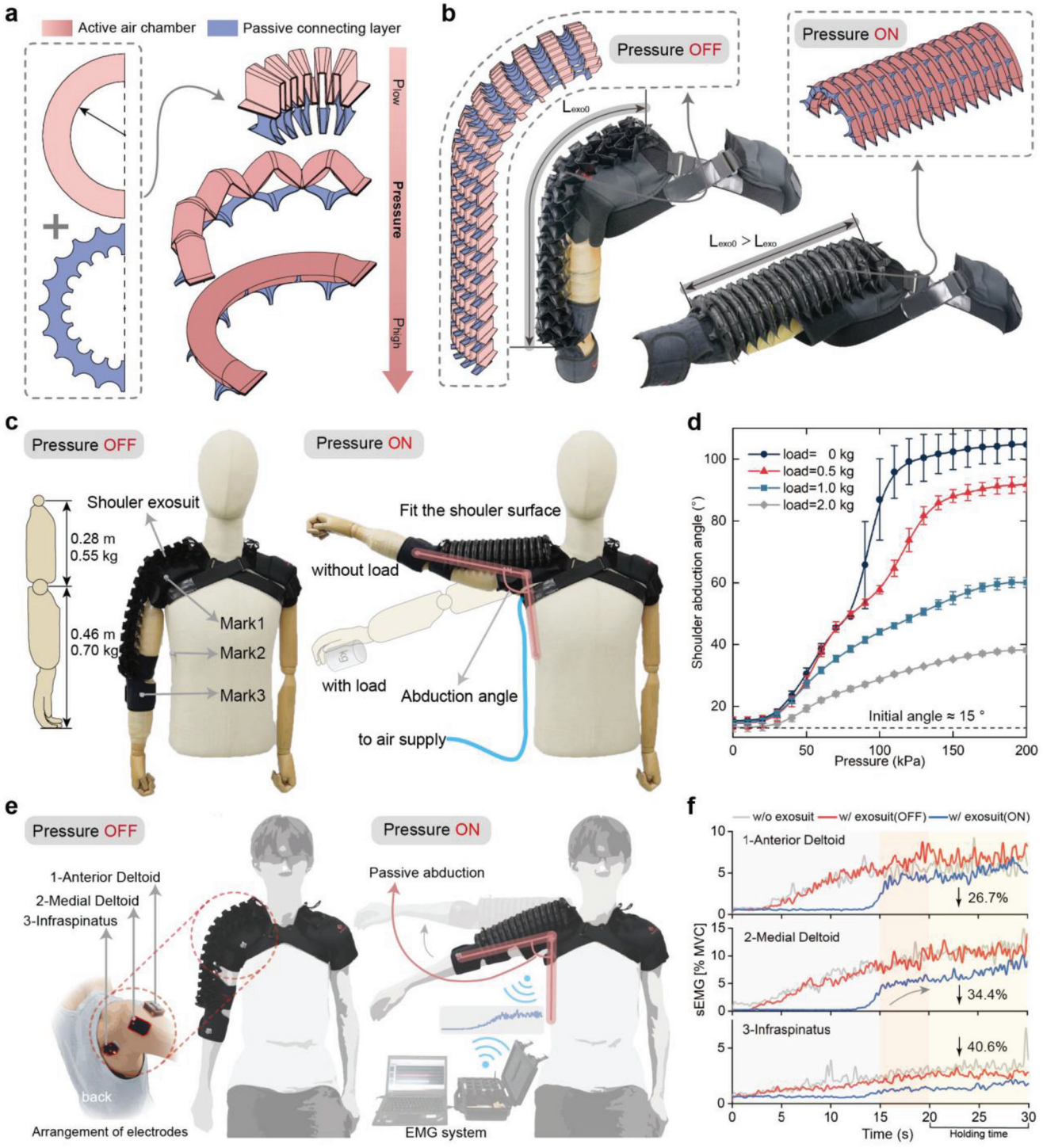

Figure 4. An assistive shoulder exosuit based on arched fabric-lattice artificial muscles (FAMs). a) Schematic diagram of a row array of the arched FAM; the air chamber and connecting layer have a semicircle shape. b) Design and working principle of the assistive shoulder exosuit. c) Verifications on a mannequin: when pressurized, the exosuit pulls the arm of the mannequin up, resulting in shoulder abduction. d) The shoulder abduction angle varies with the actuation pressure and the additional load. e) Verifications on a healthy subject: the electrodes are used to monitor the surface electromyogram (sEMG) signals of the subject during experiments. f) sEMG signals of the subject when lifting his arm to the horizontal position under three conditions: without exosuit, with exosuit (OFF), and with exosuit (ON).

activity when performing shoulder abduction under three conditions, i.e., without exosuit, with exosuit (pressure OFF), and with exosuit (pressure ON)[51] (Figure 4e, Note S10, and Movie S5, Supporting Information). Experimental results show that the muscle activity of the condition with exosuit (pressure ON) is obviously lower than that of the other two conditions (Figure 4f). Compared with the condition with exosuit (pressure OFF), its muscle activity of the anterior deltoid, the medial deltoid, and the infraspinatus (muscles related to shoulder abduction[52,53]) decrease by 26.7%, 34.4%, and 40.6% in the last 10 s (i.e., holding horizontal abduction for 10 s). These experiments validate the effectiveness of our shoulder exosuit and the configurability of our FAMs.

2.5. Application III: An Adaptive Soft Gripper Based on Cylindrical FAMs

Besides linear contraction, our FAMs can also produce radial contraction by connecting their two ends into a loop, i.e., the cylindrical FAMs (**Figure 5**a, Figure S12, and Movie S6, Supporting Information). Notably, the connecting layers in the cylindrical FAMs are designed into asymmetric patterns to reduce the internal forces in deformation. These asymmetric connecting layers allow the FAM to produce a combined motion of bending and contraction (Figure S12a,b, Supporting Information), curling itself into a loop even without bonding the two ends (Movie S6, Supporting Information). Since the cylindrical FAMs themselves cannot expand radially, we integrate ring air chambers (Figure S12d, Supporting Information) to expand the actuator.

In this application, we design an adaptive soft gripper (111.8 g) that consists of a cylindrical FAM and two ring air chambers (Figure 5b). The cylindrical FAM (including ten row arrays and each of them containing three actuation units, chamber volume = 434.2 cm^3) works as a radial contraction mechanism (RCM) to envelop the objects. The two ring air chambers (inner diameter 120 mm, chamber volume = 293.0 cm^3) on the top and bottom work as a radial expansion mechanism (REM) to open the soft gripper. Through the synergistic actions of the RCM and REM, the inner diameter of the soft gripper can vary between 15 and 100 mm (Figure 5c).

We characterize the soft gripper by the pulling force tests, where the peak force is regarded as the maximum grasping force for each condition (Figure 5d, Note S11, and Movie S7, Supporting Information). Experimental results show that the maximum grasping force increases with the actuation pressure and the diameters of 3D printed cylinders (Figure 5e). For the cylinder of 90 mm, a grasping force larger than 170 N can be achieved under 120 kPa, which demonstrates the excellent carrying capability of our soft gripper. Moreover, the soft gripper successfully grasps objects of various and irregular shapes, including the ball, cuboid, cylinder, and cone, showing its robust grasping capability (Figure 5f, Note S11, and Movie S7, Supporting Information). When integrated onto an industrial robot, the soft gripper securely transfers objects, such as a slender screwdriver and stacked items (an apple model and a magic cube) from place A to place B, proving its stability during carrying tasks (Figure 5g, Note S11, and Movie S7, Supporting Information). This excellent adaptive soft gripper also demonstrates the integrability and the variable actuation modes of our FAMs.

3. Conclusion

Lattice structures are commonly used for soft metamaterials with tuneable mechanical properties due to their large stretchability.[54,55] However, most of them are passive and cannot fully exploit their advantages. Herein, we present a method of integrating lattice structures with pneumatic actuation and design a class of active lattice actuators—FAMs that achieve large contraction ratios (up to 87.5%), which are adjustable from 0% to 100% theoretically. Different from most PAMs with sharply decreasing output force, FAMs can retain considerable output forces at large contraction ratios, resulting in the high energy density. Notably, diverse configurations and motions can be achieved with FAMs by tuning the geometry of the components, including the arched configuration, combined motion of contraction and bending, and radial contraction. Based on these excellent properties, FAMs with desired performance, configuration, and motion can be designed to enable various practical applications, such as the powerful robotic elbow, the assistive shoulder exosuit, and the adaptive soft gripper developed in this work. The FAMs can also be powered with moderate but acceptable speed by portable pumps. For example, the type IX can be inflated to 200 kPa in 8 s by a portable pump (Movie S2, Supporting Information). Therefore, these robotic applications can be integrated into untethered and portable systems (Movies S5 and S7, Supporting Information).

Compared with existing PAMs, our FAMs show remarkable comprehensive performance in terms of contraction ratio, output force, and versatility (Table S2, Supporting Information). In addition, our FAMs are controllable, rapid to respond, lightweight, inexpensive, scalable, and facile to fabricate, allowing mass manufacturing with industrial heat-sealing/pressing methods for practical applications such as wearable devices and medical instruments. However, we should mention that the required preload and inevitable transverse elongation of FAMs could impede their applications in load-free conditions and confined spaces. Besides, there is still a trade-off between the contraction ratio and output force, which limits the FAMs to possess extremely large contraction ratio and high output force concurrently when keeping the dimensions and chamber volume in acceptable ranges. For applications requiring both extremely large contraction ratio and high output force, it could be a good choice to parallel the FAMs with small $\frac{w}{l}$.

In the future, the current design can be further optimized for better performance in some aspects. For example, a connecting layer that wraps around the air chamber at their connection areas can enhance the connections to further avoid fatigue failure. Moving forward, many opportunities exist in exploring more universal design methods, more abundant configurations and actuation modes, and even 3-dimensional arrangements of actuation units for FAMs to enable more practical applications. Moreover, our design method may inspire future research in soft actuators, by inherently integrating pneumatics with large deformation but passive structures, such as origami, kirigami, and other lattice structures.

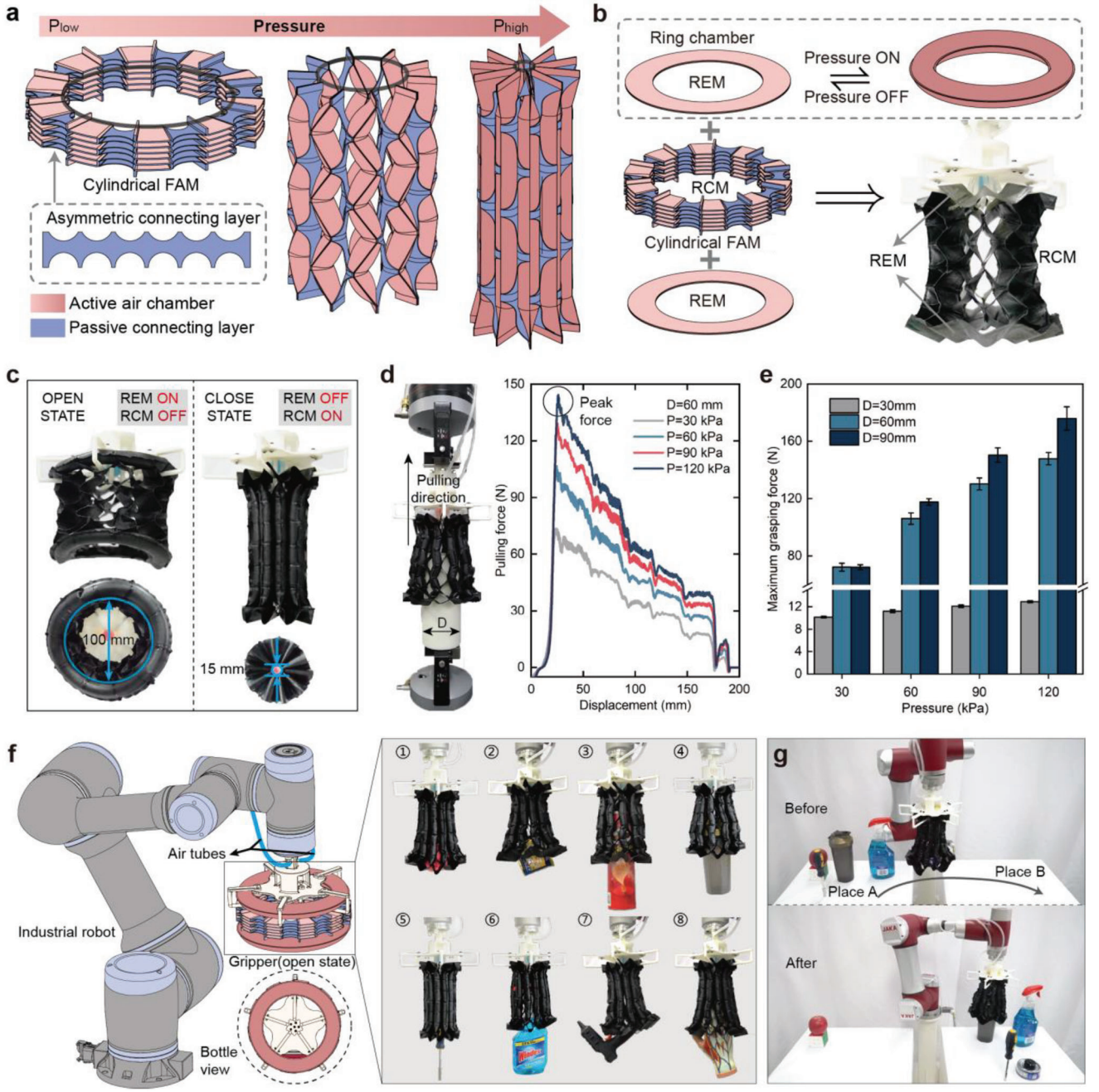

Figure 5. An adaptive soft gripper based on cylindrical fabric-lattice artificial muscles (FAMs). a) Schematic diagram of the cylindrical FAM gradually shrinking under increasing actuation pressure; the connecting layer is designed into an asymmetric pattern to reduce the internal force in deformation. b) The adaptive soft gripper is composed of a cylindrical FAM (working as a radial contraction mechanism, RCM) and two ring air chambers (working as a radial expansion mechanism, REM). c) Working principles of the adaptive soft gripper. The inner diameter of the gripper can vary between 100 and 15 mm. d) Example results of the pulling force test for the gripper, where the peak force is regarded as the maximum grasping force for each condition. e) Maximum grasping force varies with the actuation pressure and the diameter of the cylinder. f) Integrated onto an industrial robot, the gripper can adapt to the shapes of unknown objects to achieve steady grasping and g) carrying tasks.

4. Experimental Section

Materials of FAMs: Primary materials comprising FAMs are N210D Nylon fabric with TPU coated on both sides (0.4 mm, Jiaxing Yingcheng Textile Co., Ltd, China), non-stick baking paper (0.05 mm, Foshan Nanhai Weiji Kitchen Utensil Co., Ltd, China), TPU air connecter (Φ3, Shenzhen Jianda Handbag Accessories Co., Ltd, China), and silicone tubes (Φ3, Daoguan Co., Ltd., China).

Fabrication of FAMs: The main tools used to fabricate FAMs were a laser cutter (VLS 3.50, Universal Laser Systems, USA), an acrylic

bending machine (Type A, Jinan Hongyang CNC Machinery Co., Ltd., China), a heat press machine (38 × 38 cm, Yiwu Hexin Digital Technology Co., Ltd., China), and a customized heat press machine. The fabrication process of FAMs mainly contains five stages: 1) design and draw the 2D patterns of the fabric sheets and baking paper with AutoCAD (AutoDesk, USA); 2) laser cut the original materials to obtain patterned fabric sheets and baking paper; 3) fabricate the air chambers; 4) fabricate the row arrays; and 5) fabricate the FAMs. Please see the Note S2 and Movie S1 (Supporting Information) for more details.

Modeling of FAMs: For the theoretical model, the geometry of FAMs in motion was simplified to estimate the volume of the air chamber and vertical length. Then the output force of FAMs could be calculated based on the principle of virtual work. Thus, the force–contraction ratio could be obtained using numerical calculations in MATLAB (The MathWorks, Inc., USA). Please see Note S6 (Supporting Information) for more details.

Pneumatic Sources: The pneumatic control systems in this work were based on an oil-free air compressor (OTS-950×2, Taizhou Outstanding Industry & Trade Co., Ltd, China), a customized pressure regulator (12 channels, Deli Group, China), pressure sensors (MPX Series, Freescale Semiconductor, USA), and a programmable controller (microLabBox 1202, dSPACE, Germany). Connected to the air compressor (works as a high-pressure air supply) and controlled by the dSPACE controller (PID control strategy), the customized pressure regulator could produce desired pressure to the FAMs, such as constant pressure, sinusoidal pressure, and approximate step pressure. The actual pressures in all experiments were recorded.

Characterization and Application Experiments: The other devices for characterization and application experiments in this work included a laser sensor (HG-C1400-P, Panasonic, Japan), a flow sensor (MF-4003, Langfan, China), a stainless air reservoir (10 L, Comeon, China), a portable pump (NMP 850.1.2 KPDC-B HP, 24 V; 30 W, KNF Technology Co., Ltd, Germany), solenoid valves (N2V025-08 series, Chint Electric, China), a universal testing machine (68SC-2, Instron, USA), a motion capture system (Prime 13, OptiTrack, USA), a surface electromyographic acquisition system (Trigno, DELSYS INC., USA), an industrial robot (Zu 7, Jaka Co., Ltd., China), and 3D-printed components (DSM IMAGE8200 pro, WeNext Technology Co., Ltd., China). The details of the characterization and application experiments can be found in the Notes S3–S5, and S8–S11 (Supporting Information).

Statistical Analysis: Data are presented as mean values ± standard deviation with sample size as specified in the experiments. Statistical analysis was carried out using Origin and MATLAB Software.

Supporting Information

Supporting Information is available from the Wiley Online Library or from the author.

Acknowledgements

The authors thank W. Huang for his discussion in the early design and J. Sun for checking and suggesting the manuscript. This work was partially supported by the National Natural Science Foundation of China (Grant Nos. 52025057 and T2293725) and the Science and Technology Commission of Shanghai Municipality (Grant No. 22511101700).

Conflict of Interest

The authors declare no conflict of interest.

Author Contributions

D.Y. conceived the idea and contributed to experiments, modeling, data processing, and writing. M.F. assisted in experiments and writing. G.G. supervised the project and contributed to the design of experiments and writing. All the authors provided feedback and agree with the final version of the manuscript.

Data Availability Statement

The data that support the findings of this study are available in the supplementary material of this article.

Keywords

active lattice, contraction ratio, pneumatic artificial muscles, soft actuators, soft robotics

Received: July 13, 2023
Revised: August 25, 2023
Published online: November 23, 2023

[1] D. Rus, M. T. Tolley, *Nature* **2015**, *521*, 467.
[2] G. Gu, J. Zou, R. Zhao, X. Zhao, X. Zhu, *Sci. Rob.* **2018**, *3*, eaat2874.
[3] G. Li, X. Chen, F. Zhou, Y. Liang, Y. Xiao, X. Cao, Z. Zhang, M. Zhang, B. Wu, S. Yin, Y. Xu, H. Fan, Z. Chen, W. Song, W. Yang, B. Pan, J. Hou, W. Zou, S. He, X. Yang, G. Mao, Z. Jia, H. Zhou, T. Li, S. Qu, Z. Xu, Z. Huang, Y. Luo, T. Xie, J. Gu, et al., *Nature* **2021**, *591*, 66.
[4] Y. Chen, H. Zhao, J. Mao, P. Chirarattananon, E. F. Helbling, N. P. Hyun, D. R. Clarke, R. J. Wood, *Nature* **2019**, *575*, 324.
[5] T. Proietti, C. O'Neill, L. Gerez, T. Cole, S. Mendelowitz, K. Nuckols, C. Hohimer, D. Lin, S. Paganoni, C. Walsh, *Sci. Transl. Med.* **2023**, *15*, eadd1504.
[6] G. Gu, N. Zhang, H. Xu, S. Lin, Y. Yu, G. Chai, L. Ge, H. Yang, Q. Shao, X. Sheng, X. Zhu, X. Zhao, *Nat. Biomed. Eng.* **2023**, *7*, 589.
[7] T. J. Jones, E. Jambon-Puillet, J. Marthelot, P. T. Brun, *Nature* **2021**, *599*, 229.
[8] Y. Hao, S. Biswas, E. W. Hawkes, T. Wang, M. Zhu, L. Wen, Y. Visell, *IEEE Trans. Rob.* **2021**, *37*, 350.
[9] L. Zhang, H. Yan, J. Zhou, Z. Zhao, J. Huang, L. Chen, Y. Ru, M. Liu, *Adv. Mater.* **2023**, *35*, 2202193.
[10] T. Benselfelt, P. Rothemund, P. S. Lee, *Adv. Mater.* **2023**, *35*, 2300487.
[11] Y. Shi, E. Askounis, R. Plamthottam, T. Libby, Z. Peng, K. Youssef, J. Pu, R. Pelrine, Q. Pei, *Science* **2022**, *377*, 228.
[12] C. Tang, B. Du, S. Jiang, Q. Shao, X. Dong, X. J. Liu, H. Zhao, *Sci. Rob.* **2022**, *7*, eabm8597.
[13] M. Taghavi, T. Helps, J. Rossiter, *Sci. Rob.* **2018**, *3*, eaau9795.
[14] I. H. Kim, S. Choi, J. Lee, J. Jung, J. Yeo, J. T. Kim, S. Ryu, S. K. Ahn, J. Kang, P. Poulin, S. O. Kim, *Nat. Nanotechnol.* **2022**, *17*, 1198.
[15] Q. He, Z. Wang, Y. Wang, Z. Wang, C. Li, R. Annapooranan, J. Zeng, R. Chen, S. Cai, *Sci. Rob.* **2021**, *6*, eabi9704.
[16] H. Zhang, S. Oh, M. Mahato, H. Yoo, I. K. Oh, *Adv. Funct. Mater.* **2022**, *32*, 2205732.
[17] K. Choi, S. J. Park, M. Won, C. H. Park, *Smart Mater. Struct.* **2022**, *31*, 055020.
[18] X. Gao, J. Yang, J. Wu, X. Xin, Z. Li, X. Yuan, X. Shen, S. Dong, *Adv. Mater. Technol.* **2019**, *5*, 1900716.
[19] S. M. Mirvakili, I. W. Hunter, *Adv. Mater.* **2018**, *30*, 1704407.
[20] S. Tawfick, Y. Tang, *Science* **2019**, *365*, 125.
[21] D. R. Higueras-Ruiz, M. W. Shafer, H. P. Feigenbaum, *Sci. Rob.* **2021**, *6*, eabd5383.
[22] E. Acome, S. K. Mitchell, T. G. Morrissey, M. B. Emmett, C. Benjamin, M. King, M. Radakovitz, C. Keplinger, *Science* **2018**, *359*, 61.
[23] N. Kellaris, V. Gopaluni Venkata, G. M. Smith, S. K. Mitchell, C. Keplinger, *Sci. Rob.* **2018**, *3*, eaar3276.
[24] C. De Pascali, G. A. Naselli, S. Palagi, R. B. N. Scharff, B. Mazzolai, *Sci. Rob.* **2022**, *7*, eabn4155.
[25] M. X. Yang, J. Wu, W. J. Jiang, X. R. Hu, M. I. Iqbal, F. X. Sun, *Adv. Funct. Mater.* **2023**, *33*, 2210351.

[26] R. Baines, S. K. Patiballa, B. Gorissen, K. Bertoldi, R. Kramer-Bottiglio, *Adv. Mater.* **2023**, *35*, 2300535.
[27] M. Zhu, T. N. Do, E. Hawkes, Y. Visell, *Soft Rob.* **2020**, *7*, 179.
[28] C. Ching-Ping, B. Hannaford, *IEEE Trans. Rob. Autom.* **1996**, *12*, 90.
[29] B. Tondu, P. Lopez, *IEEE Control Syst.* **2000**, *20*, 15.
[30] D. Villegas, M. Van Damme, B. Vanderborght, P. Beyl, D. Lefeber, *Adv. Robot.* **2012**, *26*, 1205.
[31] B. Vanderborght, B. Verrelst, R. Van Ham, D. Lefeber, *Robotica* **2006**, *24*, 401.
[32] J. Yi, X. Chen, C. Song, Z. Wang, *Soft Rob.* **2018**, *5*, 81.
[33] D. Bruder, R. J. Wood, *IEEE Rob. Autom. Lett.* **2022**, *7*, 542.
[34] J. Kwon, S. J. Yoon, Y.-L. Park, *IEEE Trans. Rob.* **2020**, *36*, 743.
[35] N. Oh, Y. J. Park, S. Lee, H. Lee, H. Rodrigue, *Adv. Mater. Technol.* **2019**, *4*, 1800414.
[36] J. H. Jang, B. Jamil, Y. Moon, A. Coutinho, G. Park, H. Rodrigue, *IEEE–ASME Trans. Mechatron.* **2023**, 1, https://doi.org/10.1109/TMECH.2023.3244347.
[37] K. Han, N. H. Kim, D. Shin, *Soft Rob.* **2018**, *5*, 554.
[38] H. D. Yang, B. T. Greczek, A. T. Asbeck, *Front Rob. AI* **2018**, *5*, 136.
[39] F. Connolly, C. J. Walsh, K. Bertoldi, *Proc. Natl. Acad. Sci. USA* **2017**, *114*, 51.
[40] F. Connolly, P. Polygerinos, C. J. Walsh, K. Bertoldi, *Soft Rob.* **2015**, *2*, 26.
[41] S. Y. Kim, R. Baines, J. Booth, N. Vasios, K. Bertoldi, R. Kramer-Bottiglio, *Nat. Commun.* **2019**, *10*, 3464.
[42] L. Belding, B. Baytekin, H. T. Baytekin, P. Rothemund, M. S. Verma, A. Nemiroski, D. Sameoto, B. A. Grzybowski, G. M. Whitesides, *Adv. Mater.* **2018**, *30*, 1704446.
[43] T. Wang, L. Ge, G. Gu, *Sens. Actuators, A.* **2018**, *271*, 131.
[44] F. Chen, Y. Miao, G. Gu, X. Zhu, *IEEE Rob. Autom. Lett.* **2021**, *6*, 5253.
[45] J. Zou, M. Feng, N. Ding, P. Yan, H. Xu, D. Yang, N. X. Fang, G. Gu, X. Zhu, *Natl. Sci. Rev.* **2021**, *8*, nwab048.
[46] R. Zhen, L. Jiang, H. Li, B. Yang, *Soft Rob.* **2023**, *10*, 380.
[47] D. Xie, J. Liu, S. Zuo, *IEEE Rob. Autom. Lett.* **2021**, *6*, 8599.
[48] J. Liu, Z. Ma, Y. Wang, S. Zuo, *IEEE Rob. Autom. Lett.* **2022**, *7*, 8635.
[49] S. Li, D. M. Vogt, D. Rus, R. J. Wood, *Proc. Natl. Acad. Sci. USA* **2017**, *114*, 13132.
[50] J. G. Lee, H. Rodrigue, *Soft Rob.* **2019**, *6*, 109.
[51] M. Feng, D. Yang, G. Gu, *IEEE Rob. Autom Lett.* **2021**, *6*, 3105.
[52] H. J. Hermens, B. Freriks, C. Disselhorst-Klug, G. Rau, *J. Electromyogr. Kinesiol.* **2000**, *10*, 361.
[53] D. A. Neumann, *Kinesiology of the Musculoskeletal System-e-book: Foundations for Rehabilitation*, Elsevier Health Sciences, Oxford **2016**, Ch. 5.
[54] D. Wang, L. Dong, G. Gu, *Adv. Funct. Mater.* **2022**, *33*, 2208849.
[55] B. Deng, A. Zareei, X. Ding, J. C. Weaver, C. H. Rycroft, K. Bertoldi, *Adv. Mater.* **2022**, *34*, 2206238.